



ELSEVIER

Contents lists available at ScienceDirect

Cement and Concrete Composites

journal homepage: www.elsevier.com/locate/cemconcompFreeze-thaw crack determination in cementitious materials using 3D X-ray computed tomography and acoustic emission[☆]Yasmina Shields^a, Edward Garboczi^b, Jason Weiss^c, Yaghoob Farnam^{a,*}^a CAEE Department, Drexel University, Philadelphia, PA, USA^b National Institute of Standards and Technology, Boulder, CO, USA^c CCE Department, Oregon State University, Corvallis, OR, USA

ARTICLE INFO

Article history:

Received 12 September 2017
 Received in revised form
 26 February 2018
 Accepted 7 March 2018
 Available online 8 March 2018

Keywords:

3D X-Ray
 Acoustic emission
 Concrete
 Fracture
 Freeze-thaw

ABSTRACT

As concrete freezes and thaws cracks may develop. These cracks can provide a path for water and ionic species to penetrate the concrete. This may reduce the service-life of the concrete element. In this study, X-ray computed tomography (CT) was used as a non-destructive technique to characterize the microstructure of mortar samples that were exposed to different levels of freeze-thaw damage by varying degree of saturation in the samples (75, 90, 95, and 100% degrees of saturation). Acoustic emission (AE) experiments were performed during freezing and thawing to investigate sample cracking behavior. The volume of cracks present within the mortar samples after freezing and thawing were determined using X-ray CT and compared to passive acoustic emission data. The location/source of cracks was also determined using X-ray CT. The crack sources (i.e., void, aggregate, interfacial transition zone, or paste) were determined using X-ray CT and were related to AE activities during cracking. Crack volumes were found to increase with increased levels of saturation, and visual observations of cracking were found to correlate with AE signatures of various crack sources.

© 2018 Elsevier Ltd. All rights reserved.

1. Introduction

The cracking behavior of a composite system like concrete is dependent on the properties of its constituent components. Cracks can form within a concrete specimen in a variety of ways, such as an applied external force, temperature changes leading to volumetric mismatch, and internal chemical reactions usually caused by the ingress of aggressive chemicals [1,2]. Small cracks can form and eventually propagate, thus serving as a source for the development of larger cracks [2,3]. A number of nondestructive techniques have been used to better analyze cracking within concrete, such as visual inspection, microscopic analysis, 3-D X-ray computed tomography (CT), ultrasonic pulse velocity, resonant frequency, and acoustic emission [4,5]. Acoustic emission (AE) is a real-time, non-destructive evaluation method that can be used to investigate cracking in concrete [6,7]. Passive AE corresponds to soundwaves that are produced when cracks develop in a material. When a crack is formed in the concrete, energy is released and a portion of this

energy is dissipated as an acoustic wave with specific waveform signatures [8–10]. Acoustic waves and corresponding energy could be released by the formation of cracks or microcracks due to freeze-thaw cycles [11–13]. The characteristics of the acoustic waves (e.g., the number of counts, number of hits, amplitude, rise time, duration, velocity, frequency, signal strength, and corresponding AE energy) may provide a method to evaluate cracking in samples exposed to freezing and thawing [3,14]. Generally, the strength of the signals and the waveform properties depend on the amount of released energy, distance, source, and the orientation of the source with respect to the AE sensor [15]. Passive AE tests involve AE transducers that continuously sense acoustic waves generated by the formation of cracks or microcracks during a test. These acoustic waves are then analyzed to identify the type and magnitude of the resulting damage. In cementitious materials, the source of AE activities may be located within different constituents consisting of the aggregate or the matrix (cement paste and interfacial transition zones (ITZs)), and cracking in each constituent may create different types of AE activity that can be used to classify cracking type and phase location [15].

3D X-ray CT can also be leveraged as an efficient non-destructive characterization of the microstructure of mortar

[☆] Partial contribution of NIST – not subject to US copyright

* Corresponding author.

E-mail address: yfarnam@drexel.edu (Y. Farnam).

samples [16]. This method allows the user to visualize the components present within an opaque subject being analyzed as well as to obtain accurate quantitative information on the area and volume of specific components [16,17]. Additionally, X-ray micro-CT scans can be assembled into 3D models and used for finite element computations of fracture in mortar and concrete [18–21]. The images taken consist of various grey intensities that correspond to different densities within the sample, where darker shades usually correspond to low density components (i.e., voids, cracks) and lighter shades usually correspond to higher density materials (i.e., cement paste, aggregate) [16,22]. To identify air voids, a threshold intensity value can be chosen. Using a threshold value that corresponds to a gray intensity, the original image can be transformed to a binary image, which can then be used to measure the size of the components that is represented by the remaining pixels in the binary image [16,23].

The purpose of this work is to characterize the fracture behavior of the concrete by investigating the AE waveforms and comparing AE activities to visual observations obtained from 3-D X-ray computed tomography (CT). Accordingly, the fracture behavior of the individual components of the concrete (e.g., within the cement paste, aggregate and ITZ) can be identified and characterized due to freeze-thaw damage.

2. Experimental program

2.1. Materials and mixture proportioning

All tests were performed on a mortar mixture with a water-to-cement ratio (w/c) of 0.42 by mass and a sand volume fraction of 55%. The mortar contained ordinary Type I Portland cement (OPC) with a fineness of 375 m²/kg (C₃S = 60%, C₂S = 10%, C₃A = 9%, C₄AF = 10%, and Na₂O_{EQ} = 0.86%). The aggregate was natural sand with a maximum size of 4.75 mm, specific gravity of 2.61, fineness modulus of 2.89, and an absorption value of 2.2% by mass. ASTM C305-12 [24] was followed during the preparation of the samples in a standard mortar mixer. The mortar samples with dimensions of 25.4 mm × 25.4 mm × 300 mm (1 in × 1 in × 11.81 in) were cast, vibrated, and sealed for 28 d. Following curing, mortar samples were cored and cut into cylinders with a 10-mm diameter and a 20-mm length for freeze-thaw test.

The samples were placed in a vacuum oven at 50 °C ± 1 °C with a pressure of 2.66 kPa ± 0.66 kPa (20 mmHg ± 5 mmHg) for one day. The samples were placed in a desiccator using two small spacers underneath each sample to provide a small gap between the lower surface of the sample and the bottom of the container. The samples were evacuated to a pressure of 10 ± 5 mmHg for 3 h. Following evacuation but still under vacuum, de-aerated water (de-aerated by vacuuming the water for 15 min) was added to the container until the sample was completely submerged. The sample remained submerged for 1 h. Next, the submerged sample in the water was transferred to a 23 °C ± 0.5 °C chamber and remained in the chamber before testing for a period of 3 d. This condition was defined as having a 100% degree of saturation (DOS). The samples to be used for testing at lower degrees of saturation were submerged for 3 d and were then removed from the solution. The samples were set aside to dry while monitoring their mass every 1 min–5 min until the desired mass (i.e., degree of saturation) was obtained to reach the target DOS. Samples were placed in a double sealed bag for a week prior to freeze–thaw testing to assure uniform distribution of moisture within the sample. Samples with 75%, 90%, 95%, and 100% DOS were prepared in this study. The DOS was calculated by using the ratio of the volume of absorbed water to the total volume of water that the sample was capable of absorbing.

2.2. Freeze-thaw testing procedure

Freeze–thaw testing was performed on samples using a thermally insulated setup shown in Fig. 1. The temperature of the sample was controlled using a cold plate. One AE sensor was used to investigate the acoustic activity of a sample during freezing and thawing. Vacuum grease was used to attach the sensor to the sample. High vacuum silicone grease (polydimethylsiloxane, amorphous silica, dimethyl siloxane, and hydroxyl) was used that good resistance to water, chemicals, and high and low temperatures, and it was found to be stable over the temperature range of the test. A single cooling and heating cycle was applied using a cold plate whose temperature was controlled as described in Fig. 1c, with a cooling rate of 2 °C/h and a heating rate of 4 °C/h (Fig. 1c). With this setup, one-dimensional heat flow was produced using a heat sink (i.e., cold plate) and an insulated enclosure. Thermocouples were used to monitor temperature in three locations (shown in Fig. 1): on the surface of the cold plate, at the bottom of the mortar sample, and around the middle of the sample. Temperature sampling was performed at a rate of 0.05 kHz during the thermal cycle.

The acoustic emission (AE) activity produced by generation of cracks or microcracks was monitored during freeze-thaw testing. The acoustic events refer to sound waves that are produced when a material undergoes cracking, resulting in stress waves because of the energy release in a material. The detected AE can cover a wide range of inaudible and audible frequencies [25]. Therefore, a threshold value of 45 dB_{AE} was selected to filter any noise created during test. A VS375-M¹ cylindrical piezoelectric sensor (with a frequency range between 100 kHz and 700 kHz) was used to convert the captured acoustic waves into electrical signals [26]. The VS375-M was found to be a promising sensor in capturing internal cracking in cementitious materials from previous works [12,15]. The AE filtered signals through AE sensor were amplified and recorded in a data-acquisition system. A Vallen AMSY-5 acoustic emission system with the capability of wave transient recording (TR) was used [27]. Therefore, a complete waveform diagram of any captured wave could be recorded and then analyzed. The area under the absolute value of the volt-time response of the AE sensor during an AE event was calculated and considered as the “AE signal energy” that is released. This AE signal energy is proportional to the fracture energy [12,28,29]. Verification of the AE signal processor, parametric input channels and system performance are reported in Ref. [30] according to EN 13477–2:2010 [31].

2.3. 3D X-Ray micro-computed tomography (CT) procedure

Crack and void distributions within mortar samples due to freeze-thaw cycling were monitored using an X-ray micro-CT instrument. X-ray micro-CT is useful in visualizing features in the interior of solid objects so that their 3D geometry and properties can be obtained and measured accurately. The components of this measurement consist of a source and a detector, with the test specimen placed on a rotating stage between the two [16]. Before scanning, samples were first dried in a vacuum oven at 50 °C ± 1 °C and a pressure of 20 mmHg ± 5 mmHg for a day after freeze-thaw testing in order to remove the moisture for easier X-ray imaging and preventing further hydration until X-ray

¹ Certain commercial equipment and/or materials are identified in this report in order to adequately specify the experimental procedure. In no case does such identification imply recommendation or endorsement by the National Institute of Standards and Technology, nor does it imply that the equipment and/or materials used are necessarily the best available for the purpose.

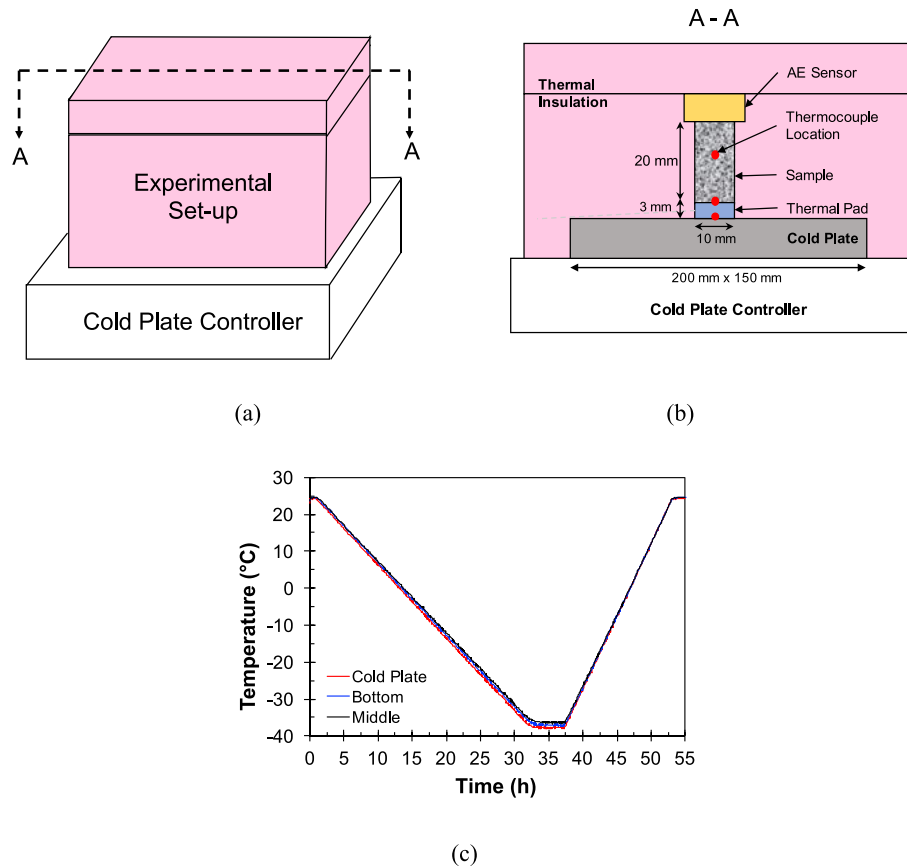


Fig. 1. (a) Experimental set-up of freeze-thaw test, (b) A-A cross section view of the experimental set-up and locations of thermocouples, (c) temperature profile at cold plate surface, bottom surface of sample, and middle of sample during freeze-thaw test.

scanning was performed. For X-ray imaging, samples were shipped to National Institute of Standards and Technology (NIST). For shipment, efforts were taken to make sure that the samples would not be disturbed.

Afterwards, X-ray images were taken of samples using a Versa XRM500 system. For 10 mm diameter mortar samples images were taken at a resolution with voxel sizes representing approximately $2.57 \mu\text{m} \times 2.57 \mu\text{m} \times 2.57 \mu\text{m}$. The field of view was taken inside the samples, approximately along the central spine and well away from either cylinder end. The X-ray source was typically operated at 80 kV and 87 μA or 7 W of power, without a filter.

X-ray imaging was performed to produce a set of CT images that could be used to generate a 3D CT image of the specimen. The resulting X-ray CT images are a map of the spatial distribution of the linear attenuation coefficients of each material phase in the sample. In this map, brighter regions correspond to higher values of the coefficient. Differentiation of features within the specimen is possible because the linear attenuation coefficient at each point depends directly on the density and composition of the specimen at that point. Thus, X-ray CT images display differences in density and composition at every point in the set of two-dimensional slices produced of the volume scanned [17,23].

To assess the likelihood of the existence of (1) initial cracks before freeze-thaw test or (2) creation of cracks due to vacuum drying, sample with 75% DOS was also tested. It has been previously shown that freeze-thaw cycles should not result in damage in samples with DOS less than critical DOS (i.e., ~85%–86%) [12,32–36].

2.4. Construction of 3D model of mortar sample using X-Ray micro-CT

To calculate void and crack volume fractions, each component (consisting of crack, voids, matrix, and aggregate) needs to be isolated for accurate data results. Image-Pro Plus software was used for image analysis in this study. This software has an array of filters and contrast adjustment features to aid in enhancing the image for analysis. Otsu's method was used for thresholding and segmentation processes [37,38]. Otsu's method involves iterating through all possible threshold values and calculates a measure of spread for the pixel gray levels on each side of the threshold (i.e., the pixels either fall in foreground or background), where the purpose is to find the threshold value where the sum of the widths of the foreground and background gray-scale distributions is at a minimum. The formula involves calculating the 'Within-Class Variance' (the sum of the foreground and background variances multiplied by their associated weights) [37].

1000 X-ray CT 2D images were stacked to construct a 3D image. Using ImagePro, the contrast and brightness levels of the images were adjusted to approximately 45–55 and 990–1000, respectively, to enhance the boundaries between the voids and cracks against various components within the mortar samples in order to accurately isolate the voids and cracks. A segmentation tool was then used to separate the voids from the background image, which would then transform the grayscale image into a binary image. Threshold values ranged between approximately 50–100. Once the stacked sequence of 1000 binary images were developed, they were modeled in 3D. The resulting 3D image was then analyzed using

counting tools to perform void volume calculations by counting the number of voxels present within the 3D reconstruction, where each voxel represented approximately $2.57 \mu\text{m} \times 2.57 \mu\text{m} \times 2.57 \mu\text{m}$.

Isolating cracks involved a dual software and manual segmentation process, where background noise and voids were erased while leaving cracks present in the image. As in the procedure to isolate voids and cracks within the images, the segmentation tool was used to isolate all the components in image that were black. This left both cracks and voids present within the image. Surface to volume ratio was used to separate cracks from voids. Since cracks possess relatively planar surfaces, they have a surface to volume ratio much higher than voids with relatively circular shape.

3. Results and discussion

3.1. Evaluation of crack origins using 3D x-ray

Cross sectional videos were made from the 3D image analysis, moving from the bottom to the top of each X-ray CT scan – links are provided as supplementary data in Appendix A, along with qualitative visual observations of each 3D image set. Additionally, 3D views of mortar samples and 2D views of critical areas are shown in Fig. 2. Cracking activity seems to increase with increasing degree of saturation (DOS) of the mortar sample. For the mortar sample with 75% DOS, (Fig. 2a), minor cracks were observed only within the ITZ regions; this may be due to the weak ITZ microstructure [39] making this zone more susceptible to damage resulted from either freeze-thaw damage or Coefficient of Thermal Expansion (CTE) mismatches between aggregate and paste than other phases. For the 90% DOS mortar sample (Fig. 2b), cracks were observed within the ITZ as well as the cement paste regions. For the 95% DOS mortar sample (Fig. 2c), cracks were observed within aggregates as well as ITZ regions. It appears that at 95% DOS, all mortar constituents (i.e., aggregate, ITZ, and cement paste) are susceptible to cracking due to freeze-thaw cycles. For the 100% DOS mortar sample (Fig. 2d) as expected, several cracks were observed in the sample that were distributed throughout all constituents of mortar sample including ITZ, paste, and aggregate.

According to the 3D image analysis, samples with DOS higher than the critical DOS (85%–86% [34,36]) had noticeable freeze-thaw damage and cracking while sample with 75% DOS (i.e., below the critical DOS) showed minor damage only in some ITZ regions. It should be mentioned that the temperature of samples in this study was decreased up to -40°C (Fig. 1c) that can result in water freezing in gel pores and create minor damage even in sample with 75% DOS [40]. Further discussion of the critical DOS will be made in Section 3.2.

Additional representative 2D images along with 3D images are provided in Fig. 2 for each of the mortar samples to emphasize the cracking in different components of the mortar; cracks were highlighted using arrows.

It should be mentioned that the X-ray CT images analyzed and provided in this study did not have more than the expected amount of noise typical to X-ray CT images [17,41–43]. It is common that X-ray CT reconstructed images contain noise. This comes from several sources. First, mortar is itself a random material. Second, there are a limited number of projections made in any CT scan, from which the cross-sectional images are mathematically produced. More projections produce less noise. Third, there are certainly random features in the mortar that are of a length scale lower than the voxel size. These will produce a source of random variation in the gray scale of the voxels, reflecting this sub-voxel scale. Finally, the filtered back-projection reconstruction algorithm used by the CT scanner we used can produce random artifacts (e.g., streaking), which often manifests itself as random noise, especially after image

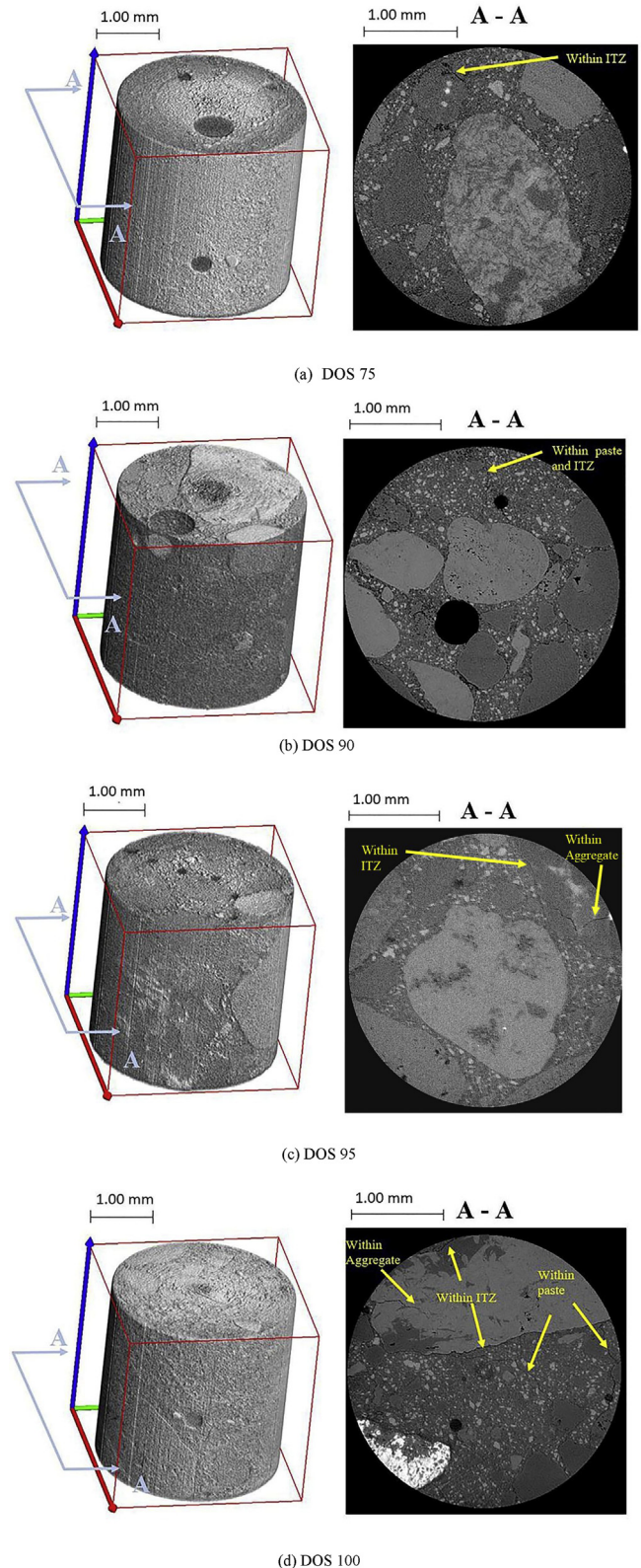


Fig. 2. 3D views of mortar samples and 2D views of critical areas of (a) DOS 75: the arrow indicates a crack observed within ITZ, (b) DOS 90: the arrow indicates a crack observed within cement paste and ITZ, (c) DOS 95: arrows indicate cracks observed within ITZ and aggregate, and (d) DOS 100: arrows indicate cracks observed within cement paste, ITZ and aggregate.

segmentation.

In this study, both low-resolution and high-resolution scanning X-ray CT methods were conducted to assess the trade-off between lowering voxel size to see more detail, and increasing voxel size, to see a greater volume of the sample. The voxel size of $2.57\ \mu\text{m}$ was found to be a satisfactory compromise to scan the necessary detail of freeze-thaw cracks over a satisfactory sample volume to be representative of the whole sample.

3.2. 3-D image analysis of crack pattern and void distribution in mortar sample with various degrees of saturation

To further investigate the effect of the degree of saturation on cracking behavior of samples during freezing and thawing, voids and cracks were isolated from the 3D image sets as shown in Fig. 3. In this figure, air voids are illustrated using red color (lighter color) while cracks due to freeze-thaw damage are illustrated using green color (darker color). As the degree of saturation increases, the number and volumes of cracks in the sample increases. The sample with 100% DOS shows several cracks throughout the sample while there is only a minor small crack observed for the 75% DOS mortar sample.

It should be mentioned that the limitations of analyzing the 3D x-ray CT image sets include the subjective image segmentation methods as well as a small mortar volume investigated. Image segmentation thresholding is highly dependent on the user and may be a potential source of error for void and crack volume calculations as it involves manually adjusting the segmentation preferences. An uncertainty analysis was performed based on the adjustment of the image segmentation thresholding preferences, yielding an uncertainty in the crack volume fraction calculation to be $\pm 0.002\ \text{mm}^3/\text{mm}^3$. In addition, only four samples were analyzed, each with a volume of about $13\ \text{mm}^3$ (higher resolution images used). It should be also mentioned that due to the limited quantity of data, a linear relationship between DOS and damage was assumed as suggested in Refs. [34,36,44]. Further investigation of more samples would provide a greater representation of the data and less uncertainty.

3.3. Acoustic emission activity during freezing and thawing

The freeze-thaw cycle in which acoustic emission activity was measured took place over an approximately 55-h period. During freezing and thawing, the AE waveform was recorded for every AE

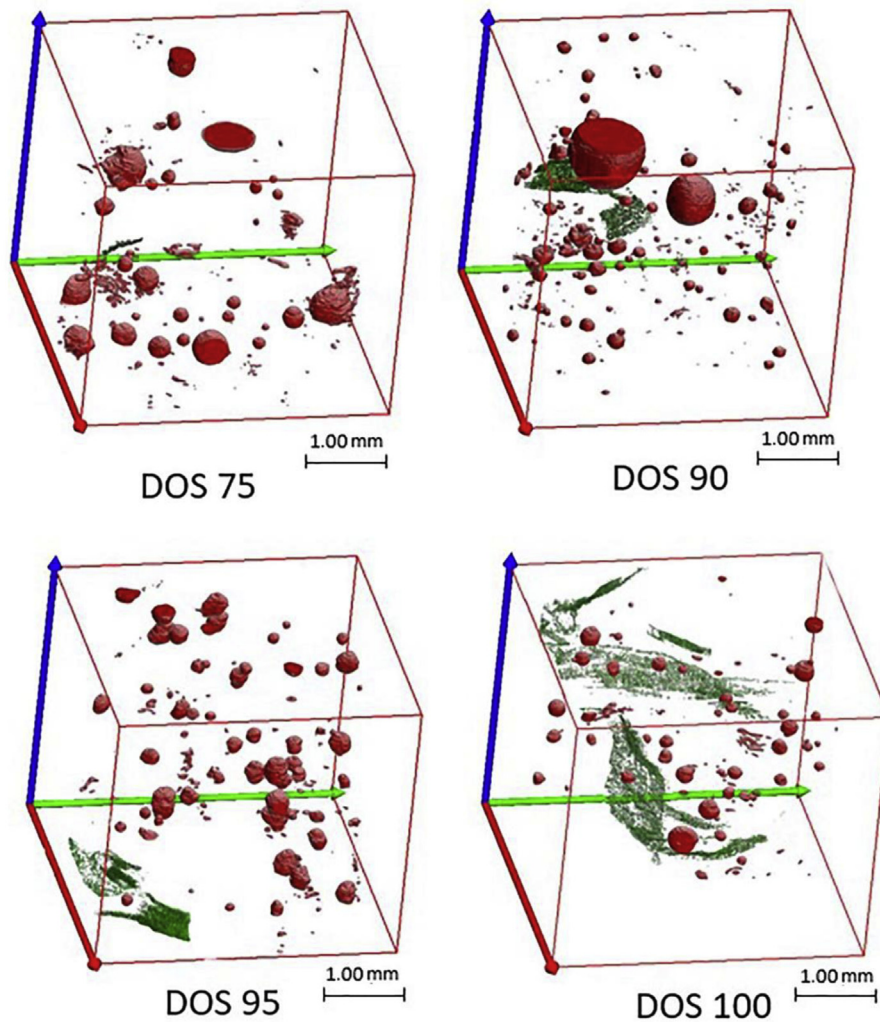


Fig. 3. 3D images of isolated cracks and voids within mortar samples with varying degrees of saturation made using X-ray micro-CT and Image-Pro Plus software: red (lighter) color indicates entrapped air voids, and green (darker) color indicates cracks due to freeze-thaw damage. (For interpretation of the references to color in this figure legend, the reader is referred to the Web version of this article.)

activity, and used to obtain AE waveform signatures. The amplitude of every AE activity and cumulative AE energy are plotted in Fig. 4 as the DOS for mortar samples varies. In Fig. 5 the final AE cumulative energy is plotted versus DOS; it appears with increasing degrees of saturation, the cumulative AE energy tends to increase within the mortar sample, which may be used as an indication of cracking damage magnitude in the sample. AE energy has been shown to be proportional to the fracture energy [5,12,14,45].

In Fig. 4, a cluster of AE activity is highlighted using an arrow for all samples that is associated with a rapid increase in AE energy at a time between 15 and 20 h. This AE activity is associated with the initiation of freezing and the formation of ice (time of freezing, t_f) in the mortar pores. The variation in the cumulative AE energy as a function of temperature was plotted Fig. 6 for samples with different DOS. Time of freezing in Fig. 6 was highlighted using a dashed line and the associated freezing temperature was reported as T_f in this plot. The AE activity that was observed before t_f in Figs. 4 and 6 is mainly attributed to the mismatch between the coefficient of thermal expansion (CTE) between aggregate and paste, as previously reported in Refs. [12,34]. It appears the AE activity due to CTE mismatch decreases as the DOS decreases, probably due to the reduction in the thermal conductivity within the sample matrix resulted from the replacement of the water with thermal conductivity of 0.5886 W/(mK) with the air with thermal conductivity of 0.023 W/(mK).

The associated T_f obtained from Fig. 6 for sample with 75% DOS is -9.3°C which is lower than freezing temperatures obtained for other samples due to mainly the capillary pore pressure effect in this sample [40]. As the DOS increases, the size of pores that are occupied by water increases. Since larger pores create lower capillary pressure, the freezing temperature (T_f) decreases as the DOS increases in the sample.

In Figs. 4 and 6, few AE activities are seen for samples with DOS below DOS_{cr} (i.e., 75% DOS) at t_f since this sample has sufficient available empty space that can be occupied by ice formation resulting in no internal pressure and damage.

In Fig. 4, another prominent gradual AE activity (highlighted using an ellipse) associated with gradual increase in AE cumulative energy in Fig. 6 is seen for all samples occurring after t_f when the

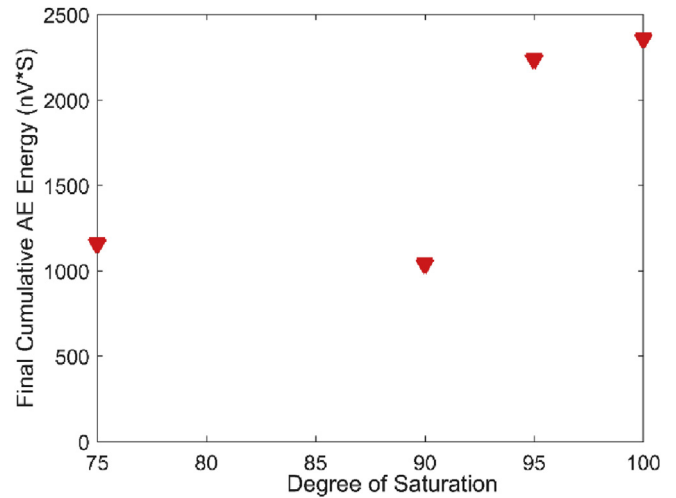


Fig. 5. The effect of DOS on the final cumulative AE energy within mortar samples subjected to freeze-thaw damage.

temperature of sample is between $\sim T_f$ and -40°C . This gradual AE activity may be due to freezing of the remaining water in mortar pores whose freezing temperature was depressed due to the effect of pore capillary pressure [40]. It should be mentioned that in a real practical situation, the likelihood of a structure experiencing a low temperature profile (near -40°C) is uncommon depending on the location of the structure in the US. In this study, the lowest temperature was set to be -40°C to monitor the freezing behavior of mortar samples in a temperature at or above -40°C . It should be noted that other temperature profiles or conditions can be applied for freezing and thawing.

3.4. Evaluation of the source of cracking using acoustic emission

It has been previously [15] shown that the AE waveforms frequency at which the spectrum has maximum amplitude (so called maximum frequency) can be used to classify the source of cracking

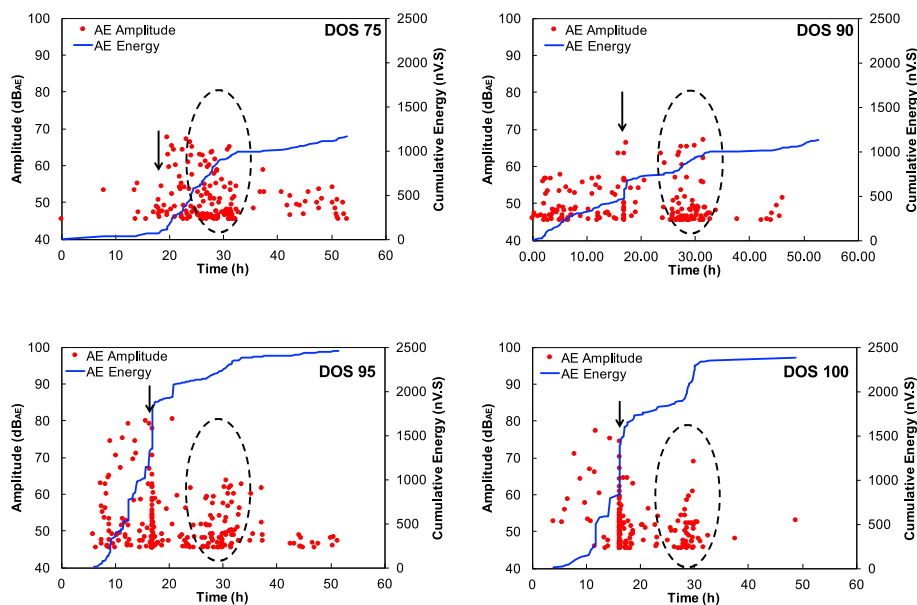


Fig. 4. Acoustic emission activity during freezing and thawing test for each DOS sample. Arrows highlight the AE activity associated with the freezing of a portion of water in the mortar pores whose freezing temperature is not influenced by pore capillary pressure, and ellipses highlight the AE activity associated with the freezing of a portion of water in the mortar pores whose freezing temperature is influenced by pore capillary pressure.

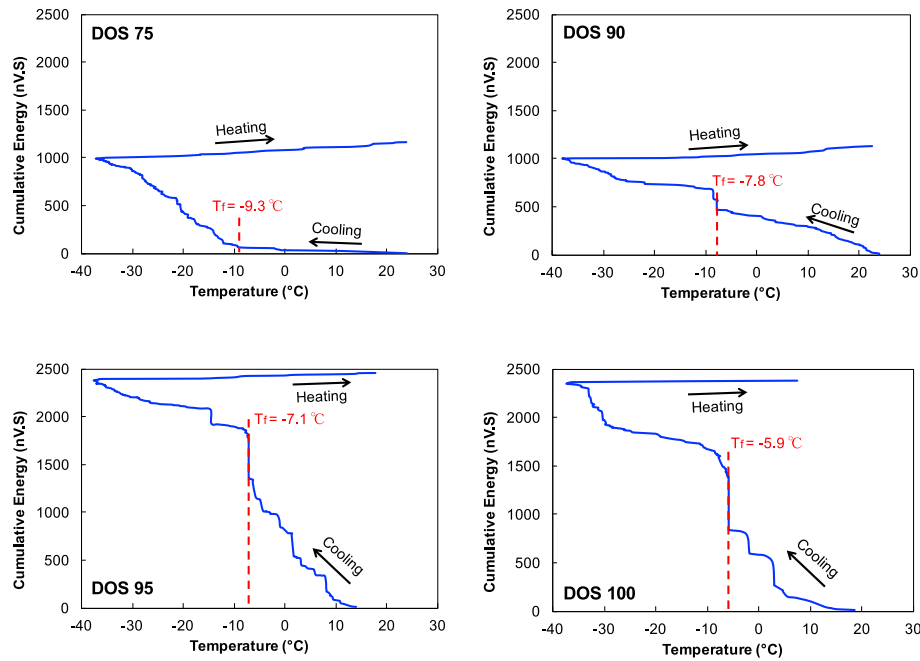


Fig. 6. AE cumulative energy as a function of temperature. Dashed line highlights the freezing temperature (T_f) or initiation of freezing event in the sample.

in mortar samples. Farnam et al. [15] showed that cracks occurring through aggregates generate AE activities with maximum frequency range between 300 kHz and 400 kHz, while cracks occurring through the matrix (paste and ITZ) have a maximum frequency range between 100 kHz and 300 kHz. This concept was used in this study to analyze the AE activity and compare the AE results with 3D x-ray CT model observations. The distribution of the cumulative AE energy as a function of AE maximum frequency was calculated with frequency bins of 20 kHz in for mortar samples with varying DOS and are shown in Fig. 7. Additionally, a vertical line was drawn in the plots to separate cracking behavior between aggregate and matrix. For samples with 75% and 90% DOS, AE activities primarily possess maximum frequencies below 300 kHz indicating cracks generated mainly from paste. As DOS increases (i.e., samples with 95% and 100% DOS), cracks appear to be generating AE waveforms with frequencies both above and below 300 kHz, indicating cracks originating from both aggregates and matrix. The AE maximum frequency analysis closely aligns with the 3D X-ray CT image observations (Table 1 in Appendix A). For samples with 75% and 90% DOS, cracks were observed mainly within matrix phases (Fig. 2a and b) while for samples with 95% and 100% DOS, cracks were observed within both matrix and aggregates (Fig. 2c and d).

3.5. The effect of degree of saturation on damage development

The volume of generated cracking due to freeze-thaw damage was calculated for each image set. The crack volumes in each sample were divided by the total analyzed volume of each 3D image set to determine a normalized percent volume of cracks present within the sample. The normalized crack volume is plotted in Fig. 8a as a function of degree of saturation. This result was also compared with the damage index (i.e., measured percent reduction in dynamic elastic modulus) associated with each degree of saturation using the AE pulse velocity technique in Fig. 8b.

A critical degree of saturation (DOS_{cr}) of 85%–86% has been suggested for freeze-thaw damage of concrete [34,36,44]. When a mortar sample possesses a DOS above DOS_{cr} , ice formation due to water freezing can create a noticeable internal pressure inside the

sample due to water freezing expansion (i.e., 9% expansion from liquid to solid phase) creating freeze-thaw damage. In samples with lower DOS than DOS_{cr} , the volume of empty spaces in concrete pores is sufficient to accommodate the 9% expansion resulting pressure as such no freeze-thaw damage is expected due to freezing. As shown in Fig. 8 and as expected [12,32–36], the sample with 75% DOS showed little crack volume and damage index in comparison to other samples. The volume of cracks and the damage index were near zero indicating that there were no considerable cracks in sample with 75% DOS that were not detected by pulse velocity or the X-ray CT scan with the voxel size used in this study.

To estimate the DOS_{cr} for the samples tested in this study, a linear curve fitting (expected from Refs. [34,36,44]) was used to fit a line for samples with DOS higher than 85% and the intersection with the horizontal axis was reported as DOS_{cr} , where the volume of crack or damage index is expected to be zero. Accordingly, the DOS_{cr} for mortar samples was found to be 86.7% when the crack volume was used to calculate DOS_{cr} and 83.8% when the damage index from AE was used to calculate DOS_{cr} . The calculated DOS_{cr} values are very close to the values estimated previously in Refs. [34,36,44], i.e., 85%–86%.

4. Summary and conclusions

This paper examines the use of 3D X-ray computed tomography (CT) and acoustic emission (AE) techniques as non-destructive methods to determine the source of cracking in samples with varying degree of saturation (DOS) exposed to freeze-thaw cycles. The crack sources, including aggregate, interfacial transition zone (ITZ) or paste, were determined in each sample after exposure to freezing and thawing using the 3D X-ray CT images. Additionally, the 3D X-ray CT observations were related to AE activities and signatures due to cracking that were monitored during freezing and thawing.

Crack volumes obtained from the 3D X-ray CT images were found to decrease with decreased DOS up to a critical DOS of 85.3%, below which crack volume was relatively negligible. Visual observations of cracking from 3D X-ray CT images were found to closely align with AE signatures of various crack sources. Using AE

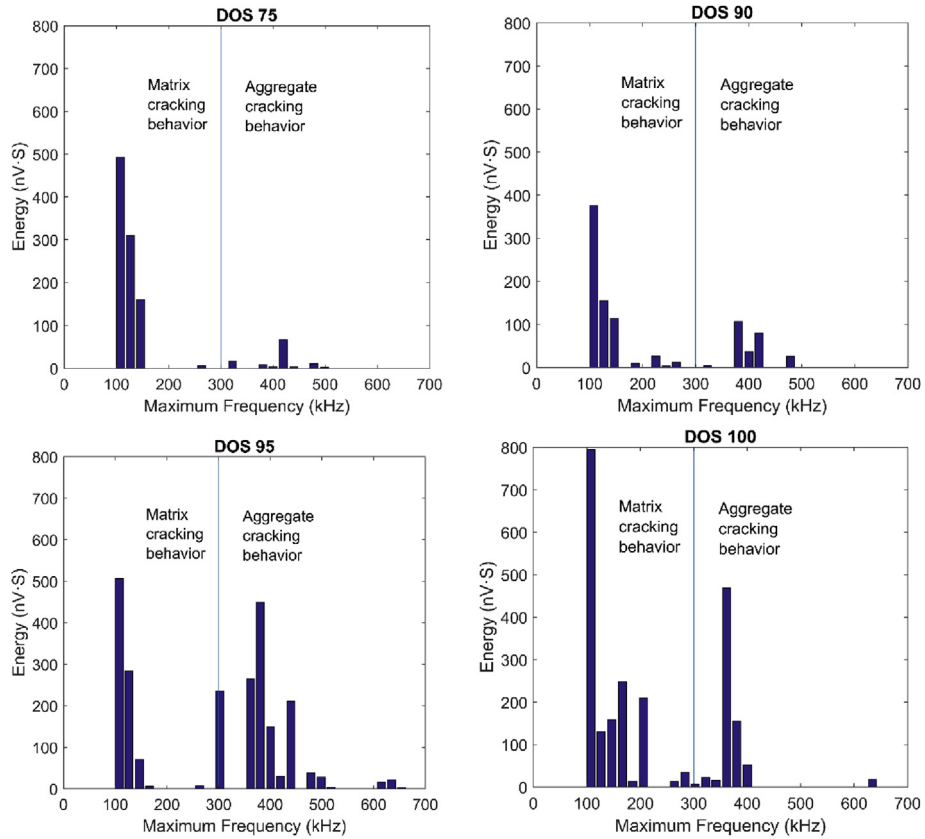


Fig. 7. The cumulative AE energy distribution associated with AE maximum frequency for mortar samples with 75%, 90%, 95%, and 100% DOS.

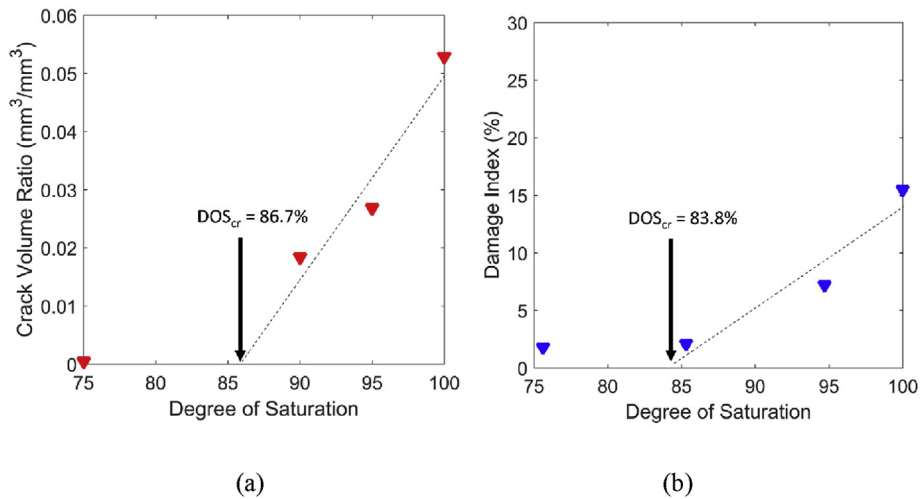


Fig. 8. The effect of DOS on (a) the volume of crack generated obtained using 3D x-ray CT images due to freeze-thaw damage on mortar samples, and (b) damage index (reduction in relative dynamic elastic modulus) obtained from AE pulse velocity test. The dotted lines are linear fits to the data with DOS above 85%.

maximum frequency analysis and visual observations from the 3D X-ray CT images, it was found that aggregate cracking as well as matrix (i.e., ITZ and paste) cracking were more prominent in mortars with higher degrees of saturation (DOS = 95% and 100%). For samples with lower degrees of saturations (DOS = 75% and 90%), only matrix cracking was found. X-ray CT analysis, at the resolution employed in this study (2.57 $\mu\text{m} \times 2.57 \mu\text{m} \times 2.57 \mu\text{m}$), supports the results obtained from AE measurement. Both techniques can detect the change in cracking behavior and its source as the degree of saturation varies in mortar samples.

Limitations to this research include the limited quantity of data, the linear curve fitting between DOS and damage and limitations in proper estimation of uncertainty. Further investigation of more samples would provide a greater representation of the data and less uncertainty.

Appendix B. Supplementary data

Supplementary data related to this article can be found at <https://doi.org/10.1016/j.cemconcomp.2018.03.004>.

APPENDIX A

Table 1

Sources of cracks in mortar samples due to freezing and thawing observed in the 3D X-ray CT image analysis.

Degree of Saturation in Mortar Sample (%)	Cracking Observations from 3D X-ray within Mortar Constituents			Video link
	ITZ	Hydrated Paste	Aggregate	
75	Minor	–	–	Video 1: vimeo.com/219058154
90	Yes	Yes	–	Video 2: vimeo.com/219057629
95	Yes	–	Yes	Video 3: vimeo.com/219058146
100	Yes	Yes	Yes	Video 4: vimeo.com/219058164

References

- [1] Z. Li, S.P. Shah, Localization of microcracking in concrete under uniaxial tension, *ACI Mater. J.* 91 (1994) 372–381.
- [2] G.C. Sih, A. DiTommaso, *Fracture Mechanics of Concrete: Structural Application and Numerical Calculation*, Springer Netherlands, Dordrecht, Netherlands, 1984, <https://doi.org/10.1007/978-94-009-6152-4>.
- [3] S. Puri, J. Weiss, Assessment of localized damage in concrete under compression using acoustic emission, *J. Mater. Civ. Eng.* 18 (2006) 325–333, [https://doi.org/10.1061/\(ASCE\)0899-1561\(2006\)18:3\(325\)](https://doi.org/10.1061/(ASCE)0899-1561(2006)18:3(325)).
- [4] Z. Yang, *Assessing Cumulative Damage in Concrete and Quantifying its Influence on Life Cycle Performance Modeling*, Purdue Univ, 2004.
- [5] M. Pour-Ghaz, *Detecting Damage in Concrete Using Electrical Methods and Assessing Moisture Movement in Cracked Concrete*, Purdue University, 2011.
- [6] Y. D-J, Detecting the extent of corrosion with acoustic emission, *Transport. Res. Rec.* (2000) 54–60.
- [7] A. Farhidzadeh, E. Dehghan-Niri, S. Salamone, B. Luna, A. Whittaker, Monitoring crack propagation in reinforced concrete shear walls by acoustic emission, *J. Struct. Eng.* 139 (2013) 1–10, [https://doi.org/10.1061/\(ASCE\)ST.1943-541X.0000781](https://doi.org/10.1061/(ASCE)ST.1943-541X.0000781).
- [8] S. Yuyama, Z. Li, Y. Ito, M. Arazoe, Quantitative analysis of fracture process in RC column foundation by moment tensor analysis of acoustic emission, *Construct. Build. Mater.* 13 (1999) 87–97, [https://doi.org/10.1016/S0950-0618\(99\)00011-2](https://doi.org/10.1016/S0950-0618(99)00011-2).
- [9] L. Qin, H.W. Ren, B.Q. Dong, F. Xing, Acoustic emission behavior of early age concrete monitored by embedded sensors, *Materials* 7 (2014) 6908–6918, <https://doi.org/10.3390/ma7106908>.
- [10] M. Ohtsu, M. Shigeishi, Y. Sakata, Nondestructive evaluation of defects in concrete by quantitative acoustic emission and ultrasonics, *Ultrasonics* 36 (1998) 187–195, [https://doi.org/10.1016/S0041-624X\(97\)00091-7](https://doi.org/10.1016/S0041-624X(97)00091-7).
- [11] J. Ranz, S. Aparicio, H. Romero, M.J. Casati, M. Molero, M. González, Monitoring of freeze-thaw cycles in concrete using embedded sensors and ultrasonic imaging, *Sensors* 14 (2014) 2280–2304, <https://doi.org/10.3390/s140202280>.
- [12] Y. Farnam, D. Bentz, A. Sakulich, D. Flynn, J. Weiss, Measuring freeze and thaw Damage in mortars containing deicing salt using a low-temperature longitudinal guarded comparative calorimetric and acoustic emission, *Adv. Civ. Eng. Mater.* 3 (2014) 316–337, <https://doi.org/10.1520/ACEM20130095>.
- [13] T. De Kock, M.A. Boone, T. De Schryver, J. Van Stappen, H. Derluyn, B. Masschaele, G. De Schutter, V. Cnudde, A pore-scale study of fracture dynamics in rock using x-ray micro-CT under ambient freeze–thaw cycling, *Environ. Sci. Technol.* 49 (2015) 2867–2874, <https://doi.org/10.1021/es505738d>.
- [14] E.N. Landis, L. Baillon, Experiments to relate acoustic emission energy to fracture energy of concrete, *J. Eng. Mech.* 128 (2002) 698–702, [https://doi.org/10.1061/\(ASCE\)0733-9399\(2002\)128:6\(698\)](https://doi.org/10.1061/(ASCE)0733-9399(2002)128:6(698)).
- [15] Y. Farnam, M.R. Geiker, D. Bentz, J. Weiss, Acoustic emission waveform characterization of crack origin and mode in fractured and ASR damaged concrete, *Cement Concr. Compos.* 60 (2015) 135–145, <https://doi.org/10.1016/j.cemconcomp.2015.04.008>.
- [16] E. Masad, V.K. Jandhyala, N. Dasgupta, N. Somadevan, N. Shashidhar, Characterization of air void distribution in asphalt mixes using x-ray computed tomography, *J. Mater. Civ. Eng.* 14 (2002) 122–129, [https://doi.org/10.1061/\(ASCE\)0899-1561\(2002\)14:2\(122\)](https://doi.org/10.1061/(ASCE)0899-1561(2002)14:2(122)).
- [17] J.A. Slotwinski, E.J. Garboczi, K.M. Hebenstreit, Porosity measurements and analysis for metal additive manufacturing process control, *J. Res. Natl. Inst. Stand. Technol.* 119 (2014) 494, <https://doi.org/10.6028/jres.119.019>.
- [18] H.-K. Man, J.G.M. Mier, Size effect on strength and fracture energy for numerical concrete with realistic aggregate shapes, *Int. J. Fract.* 154 (2008) 61–72, <https://doi.org/10.1007/s10704-008-9270-y>.
- [19] H.-K. Man, J.G.M. van Mier, Damage distribution and size effect in numerical concrete from lattice analyses, *Cement Concr. Compos.* 33 (2011) 867–880, <https://doi.org/10.1016/j.cemconcomp.2011.01.008>.
- [20] Y. Huang, Z. Yang, W. Ren, G. Liu, C. Zhang, 3D meso-scale fracture modelling and validation of concrete based on in-situ X-ray Computed Tomography images using damage plasticity model, *Int. J. Solid Struct.* 67–68 (2015) 340–352, <https://doi.org/10.1016/j.ijsolstr.2015.05.002>.
- [21] W. Ren, Z. Yang, R. Sharma, C. Zhang, P.J. Withers, Two-dimensional X-ray CT image based meso-scale fracture modelling of concrete, *Eng. Fract. Mech.* 133 (2015) 24–39, <https://doi.org/10.1016/j.engfracmech.2014.10.016>.
- [22] A. Qsymah, R. Sharma, Z. Yang, L. Margetts, P. Mummary, Micro X-ray computed tomography image-based two-scale homogenisation of ultra high performance fibre reinforced concrete, *Construct. Build. Mater.* 130 (2017) 230–240, <https://doi.org/10.1016/j.conbuildmat.2016.09.020>.
- [23] K.Y. Kim, T.S. Yun, J. Choo, D.H. Kang, H.S. Shin, Determination of air-void parameters of hardened cement-based materials using X-ray computed tomography, *Construct. Build. Mater.* 37 (2012) 93–101, <https://doi.org/10.1016/j.conbuildmat.2012.07.012>.
- [24] ASTM C305, Standard Practice for Mechanical Mixing of Hydraulic Cement Pastes and Mortars of Plastic Consistency, ASTM Int, 2012. <https://doi.org/10.1520/C0305-12>.
- [25] M. Pour-ghaz, R. Spragg, J. Castro, J. Weiss, Can acoustic emission be used to detect alkali silica reaction earlier than length change?, in: 14th Int. Conf. Alkali-aggregate React University of Texas, Austin, Texas, 2012, pp. 1–10.
- [26] H. Vallen, AE testing fundamentals, equipment, applications, *J. Nondestruct. Testing(Germany)* 7 (2002) 1–30.
- [27] Vallen, *Acoustic Emission System AMSY-5 System Description*, 2009.
- [28] B.K. Raghun Prasad, R. Vidya Sagar, Relationship between AE energy and fracture energy of plain concrete beams: experimental study, *J. Mater. Civ. Eng.* 20 (2008) 212–220, [https://doi.org/10.1061/\(ASCE\)0899-1561\(2008\)20:3\(212\)](https://doi.org/10.1061/(ASCE)0899-1561(2008)20:3(212)).
- [29] L. Youyuan, L. Zongjin, Study of the relationship between concrete fracture energy and AE signal energy under uniaxial compression, *J. Mater. Civ. Eng.* 24 (2012) 538–547, [https://doi.org/10.1061/\(ASCE\)MT.1943-5533.0000418](https://doi.org/10.1061/(ASCE)MT.1943-5533.0000418).
- [30] Vallen, Verification of the AE Signal Processor, Parametric Input Channels and System Performance According to EN 13477-2 vol. 2017, 2010. Munich, Germany, www.vallen.de.
- [31] EN, BS EN 13477-2, Non-destructive testing. Acoustic emission. Equipment characterisation. Verification of operating characteristic, in: European Committee for Standardization 2010, 2010, p. 34.
- [32] G. Fagerlund, The significance of critical degrees of saturation at freezing of porous and brittle materials, in: Conf. Durab. Concr. ACI STP, Ottawa, Ontario, 1975, pp. 13–65.
- [33] G. Fagerlund, The international cooperative test of the critical degree of saturation method of assessing the freeze/thaw resistance of concrete, *Mater. Construcción* 10 (1977) 231–253, <https://doi.org/10.1007/BF02478694>.
- [34] W. Li, M. Pour-Ghaz, J. Castro, J. Weiss, Water absorption and critical degree of saturation relating to freeze-thaw damage in concrete pavement joints, *J. Mater. Civ. Eng.* 24 (2012) 299–307, [https://doi.org/10.1061/\(ASCE\)MT.1943-5533.0000383](https://doi.org/10.1061/(ASCE)MT.1943-5533.0000383).
- [35] G. Fagerlund, A service life model for internal frost damage in concrete, *Div. Build. Mater. Report TVB* (2004) 1–48.
- [36] Y. Farnam, H. Todak, R. Spragg, J. Weiss, Electrical response of mortar with different degrees of saturation and deicing salt solutions during freezing and thawing, *Cement Concr. Compos.* 59 (2015) 49–59, <https://doi.org/10.1016/j.cemconcomp.2015.03.003>.
- [37] S.-B. Zhou, A.-Q. Shen, G.-F. Li, Concrete image segmentation based on multiscale mathematic morphology operators and otsu method, *Ann. Mater. Sci. Eng.* 2015 (2015) 1–11, <https://doi.org/10.1155/2015/208473>.
- [38] Z. Yang, W. Ren, R. Sharma, S. McDonald, M. Mostafavi, Y. Vertyagina, T.J. Marrow, In-situ X-ray computed tomography characterisation of 3D fracture evolution and image-based numerical homogenisation of concrete, *Cement Concr. Compos.* (2017), <https://doi.org/10.1016/j.cemconcomp.2016.10.001>.
- [39] S. Diamond, J. Huang, The ITZ in concrete – a different view based on image analysis and SEM observations, *Cement Concr. Compos.* 23 (2001) 179–188, [https://doi.org/10.1016/S0958-9465\(00\)00065-2](https://doi.org/10.1016/S0958-9465(00)00065-2).
- [40] H.S. Esmaeili, Y. Farnam, D.P. Bentz, P.D. Zavattieri, W.J. Weiss, Numerical simulation of the freeze–thaw behavior of mortar containing deicing salt

- solution, *Mater. Struct.* 50 (2017) 96, <https://doi.org/10.1617/s11527-016-0964-8>.
- [41] E.J. Garboczi, Quantifying particle shape in 3D, in: *Adv. Comput. Tomogr. Geomaterials*, John Wiley & Sons, Inc., Hoboken, NJ, USA, 2013, pp. 93–100, <https://doi.org/10.1002/9781118557723.ch11>.
- [42] E.J. Garboczi, Three-dimensional mathematical analysis of particle shape using X-ray tomography and spherical harmonics: application to aggregates used in concrete, *Cement Concr. Res.* 32 (2002) 1621–1638, [https://doi.org/10.1016/S0008-8846\(02\)00836-0](https://doi.org/10.1016/S0008-8846(02)00836-0).
- [43] E.J. Garboczi, J.W. Bullard, 3D analytical mathematical models of random star-shape particles via a combination of X-ray computed microtomography and spherical harmonic analysis, *Adv. Powder Technol.* 28 (2017) 325–339, <https://doi.org/10.1016/j.apt.2016.10.014>.
- [44] G. Fagerlund, The significance of critical degrees of saturation at freezing of porous and brittle materials, in: *Durab. Concr. ACI SP-47*, OTTAWA, 1973, pp. 13–66, <https://doi.org/10.14359/17604>.
- [45] H. Shimada, K. Sakai, G.G. Litvan, Acoustic emissions of mortar subjected to freezing and thawing, in: *Second Int. Conf. Durab. Concr., Montreal, Canada, 1991*, pp. 263–278.